

Energy Spectrum Analysis on a Red Blood Cell Model

Tetsuya Yamamoto^{a)} and Hiroshi Watanabe

*Department of Applied Physics and Physico-Informatics,
Faculty of Science and Technology, Keio University, Yokohama,
Kanagawa 223-8522, Japan*

It is important to understand the dynamics of red blood cells (RBCs) in blood flow. This requires the formulation of coarse-grained RBC models that reproduce the hydrodynamic properties of blood accurately. One of the models that successfully reproduce the rheology and morphology of blood has been proposed by Fedosov *et al.* [D. A. Fedosov, B. Caswell, and G. E. Karniadakis, *Comput. Methods Appl. Mech. Eng.* **199**, 1937–1948 (2010)]. The proposed RBC model contains several parameters whose values are determined either by various experiments or physical requirements. In this study, we developed a new method of determining the parameter values precisely from the fluctuations of the RBC membrane. Specifically, we studied the relationship between the spectra of the fluctuations and model parameters. Characteristic peaks were observed in the spectra, whose peak frequencies were dependent on the parameter values. In addition, we investigated the spectra of the radius of gyration. We identified the peaks originating from the spring potential and the volume-conserving potential appearing in the spectra. These results lead to the precise experimental determination of the parameters used in the RBC model.

^{a)}Electronic mail: tyamamoto-st@keio.jp

I. INTRODUCTION

Blood has important functions in the human body such as carrying oxygen and nutrients. In recent years, blood is increasingly regarded as a promising medium to transport drugs using micro- and nano-carriers¹. The main component of blood is the red blood cells (RBCs), whose properties change in the presence of diseases such as malaria and sickle cell disease^{2,3}. Therefore, understanding the properties of RBCs in blood flow is crucial in the diagnosis and treatment of diseases, as well as the design of efficient drug carriers. Research in this field had been limited to experimental and theoretical studies. However, numerical methods capable of simulating blood flow were successively developed in the 1990s and thereafter⁴⁻¹⁰. This opened up new ways to study the rheology, morphology, and dynamics of RBCs.

Among the most adopted numerical methods of simulating RBCs are dissipative particle dynamics (DPD)^{4,5}, the lattice Boltzmann method (LBM)⁶, multiparticle collision dynamics (MPC)⁷, and smoothed particle hydrodynamics (SPH)⁸ simulations. We refer the readers to some reviews for further details on these methods^{9,10}. In DPD simulations of RBCs, for the degrees of freedom of all cell structures—the cell membrane, cytoskeleton, cytoplasm, and blood plasma—the structures are treated as Lagrangian particles. This approach enables us to flexibly and straightforwardly simulate complex fluids, keeping the conservation laws of hydrodynamics¹⁰.

In DPD models of RBCs, several parameters are determined to link the macroscopic properties of RBCs with the microscopic properties of DPD particles. Macroscopic quantities of the RBC membrane include the shear modulus and bending rigidity, which have been measured experimentally using optical tweezers and by atomic force microscopy and micropipette aspiration¹¹⁻¹⁴. However, in the case of the shear modulus for instance, its values have been determined to be 4–9 $\mu\text{N}/\text{m}$ using optical tweezers, whereas micropipette aspiration experiments have yielded values of 5–12 $\mu\text{N}/\text{m}$ ¹⁵. Because of the limited accuracy of experimental measurements, the model parameters cannot be determined accurately. In addition, the discretization of the RBC membrane further causes the uncertainty of the model parameters.

To address the above issues, we propose a new method of determining the model parameters precisely from the fluctuations of the RBC membrane. First observed in the 19th century, the fluctuations of the RBC membrane have been extensively studied especially

with regard to their origins¹⁶. Thermal fluctuations have been studied in terms of the membrane displacement and its Fourier spectrum by Gögler *et al.*¹⁷ On the other hand, Turlier *et al.*¹⁸ found that non-equilibrium fluctuations due to cell metabolism violate the fluctuation–dissipation relation. Interferometric optical tweezer techniques employed in these studies enable the measurement of RBC membrane fluctuations with sub-nanometer precision in the frequency range of $10^{-1} - 10^5$ Hz. Once measured, the membrane fluctuations can be analyzed in the frequency domain through Fourier transforms. In the case of a DPD model of RBCs, the Fourier spectra of the fluctuations are dependent on the model parameters governing the membrane properties. In the present study, we adopted the DPD model proposed by Fedosov *et al.*¹⁵ to study its fluctuation-induced spectra in detail. We measured the Fourier spectra of the fluctuations of potential energies and identified which peaks in the spectra originated from which parameters. We also measured the spectra of membrane displacement, which is measurable by experiments. These steps provide a numerical basis with which experimental results can be compared to determine the DPD model parameters.

The rest of the paper is organized as follows. In Sec. II, we describe the model of the RBC membrane. The results are described in Sec. III. Sec. IV is devoted to the summary and discussion.

II. METHOD

A. Modeling of a single RBC

1. *Shaping of the RBC membrane*

The shape of the RBC membrane was determined as follows. First, each face of a regular icosahedron was split into smaller regular triangles, and the resulting vertices were moved radially to the surface of a sphere. Each vertex was then stereographically projected onto a plane. The vertices were subjected to Delaunay triangulation to obtain a list of points (particles) comprising each regular triangle. Finally, the sphere was formed into the shape of an RBC membrane according to the following equation¹⁹:

$$z = \pm D_0 \sqrt{1 - \frac{4(x^2 + y^2)}{D_0^2}} \left[a_0 + a_1 \frac{x^2 + y^2}{D_0^2} + a_2 \frac{(x^2 + y^2)^2}{D_0^4} \right]. \quad (1)$$

Here, $D_0 = 7.82 \mu\text{m}$ is the diameter of the RBC, and the constants are $a_0 = 0.0518$, $a_1 = 2.0026$, and $a_2 = -4.491$. We chose the number of particles $N = 492$ from the fact that the RBC membrane is widely discretized using $N = 500$ in various simulations^{15,20,21}. As noted in Appendix A, we confirm that the degree of coarse graining, i.e., the number of membrane particles, has little effect on the observed peak frequencies.

Figure 1 shows the orientation of the RBC in Cartesian coordinates. We chose the z -axis as the axis of rotational symmetry of the RBC and the xy -plane perpendicular to it.

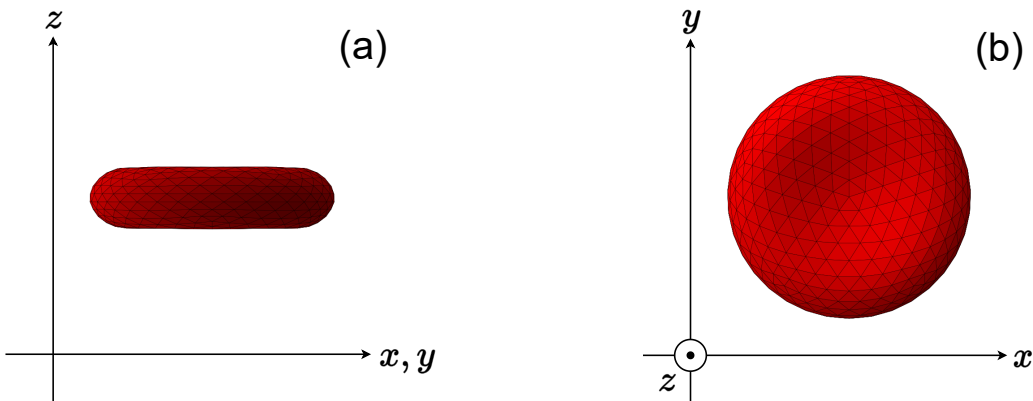


FIG. 1: (Color online) Orientation of the RBC in Cartesian coordinates. (a) Side and (b) top views of the RBC.

2. RBC membrane potentials

In this section, we consider the potentials governing the membrane particles. The total potential energy V_{RBC} is written as

$$V_{\text{RBC}} = V_{\text{spring}} + V_{\text{area}} + V_{\text{volume}} + V_{\text{bending}}. \quad (2)$$

In the following, we will outline the individual potentials. See the paper by Fedosov *et al.* for more details¹⁵. The values of the parameters involving the potentials are listed in Table I at the end of this section.

First, V_{spring} acts on the two particles making up each side of a triangular lattice. This

potential corresponds to spring forces that respond to external stress and is given by

$$V_{\text{spring}} = - \underbrace{\sum_{j=1}^{N_s} \frac{k_s}{2} (l_j^m)^2 \log(1 - x_j^2)}_{V_{\text{FENE}}} + \underbrace{\sum_{j=1}^{N_s} \frac{k_p^j}{l_j}}_{V_{\text{POW}}}, \quad (3)$$

where the first term is the finitely extensible nonlinear elastic (FENE) potential V_{FENE} ²². This potential yields attractive forces, whereas the second-term V_{POW} is a repulsive potential. N_s is the number of springs, l_j is the length of the j th spring, l_j^m is its maximum length, and $x_j = l_j/l_j^m$. k_s is a constant set to the same value for all springs. k_p^j is set individually for each spring so that the spring forces cancel out at the equilibrium length l_j^0 . In this study, l_j^0 was set equal to l_j at the RBC's initial state as shown in Fig. 1. Then, l_j^m was determined by fixing the ratio $x_0 = l_j^0/l_j^m$ for all springs. The values of k_s and k_p^j are determined from the membrane shear modulus measured by experiments^{15,23,24}.

The RBC membrane is nearly incompressible; it maintains constant surface area and volume regardless of its shape²⁵. This is reflected in the model through the area-conserving potential V_{area} and the volume-conserving potential V_{volume} . The potentials are written as

$$V_{\text{area}} = \frac{k_a (A_t^{\text{tot}} - A_0^{\text{tot}})^2}{2A_0^{\text{tot}}}, \quad (4)$$

$$V_{\text{volume}} = \frac{k_v (V_t^{\text{tot}} - V_0^{\text{tot}})^2}{2V_0^{\text{tot}}}, \quad (5)$$

where k_a and k_v are constants, A_0^{tot} is the initial area, and V_0^{tot} is the initial volume. A_t^{tot} and V_t^{tot} are the area and volume at time t , which are constrained to A_0^{tot} and V_0^{tot} , respectively. The coefficients k_a and k_v are respectively set to $315 \mu\text{N/m}$ and 1.23 kPa , which are large enough to provide a nearly incompressible membrane.

The characteristic biconcave shape of the RBC is maintained by the bending energy of the membrane²⁵. It is introduced in the model as V_{bending} given by

$$V_{\text{bending}} = \sum_{j=1}^{N_s} k_b [1 - \cos(\theta_j - \theta_0)], \quad (6)$$

where k_b is a constant and θ_j is the dihedral angle between the two triangular lattices sharing the j th edge. θ_0 is the spontaneous angle, which is often set to $\theta_0 = 0$ in the literature as is the case in this study^{18,21,26}. The coefficient k_b is derived from experimental measurements of the bending rigidity of the membrane^{15,23,24}.

From the potentials defined above, the conservative force \mathbf{F}_i^{C} acting on the i th particle is given by

$$\begin{aligned}\mathbf{F}_i^{\text{C}} &= -\nabla_i V_{\text{RBC}} \\ &= -\nabla_i (V_{\text{spring}} + V_{\text{area}} + V_{\text{volume}} + V_{\text{bending}}).\end{aligned}\quad (7)$$

The equations of each nodal force are described in Appendix B.

B. Dissipative particle dynamics

In this study, we adopted dissipative particle dynamics (DPD) to regulate the temperature of the RBC model. DPD is a stochastic thermostat similar to the Langevin thermostat, although the former conserves the total translational and angular momenta. The equations of motion for the i th DPD particle are written as⁵

$$\begin{aligned}m\dot{\mathbf{v}}_i &= \sum_{j \neq i} \mathbf{F}_{ij}^{\text{C}} + \sum_{j \neq i} \mathbf{F}_{ij}^{\text{D}} + \sum_{j \neq i} \mathbf{F}_{ij}^{\text{R}}, \\ \left\{ \begin{aligned} \mathbf{F}_{ij}^{\text{D}} &= -\gamma\omega^{\text{D}}(r_{ij})(\mathbf{v}_{ij} \cdot \mathbf{e}_{ij})\mathbf{e}_{ij}, \\ \mathbf{F}_{ij}^{\text{R}} &= \sigma\omega^{\text{R}}(r_{ij})\xi_{ij}\mathbf{e}_{ij}, \end{aligned} \right. \quad (8)\end{aligned}$$

where $\mathbf{F}_{ij}^{\text{C}}$, $\mathbf{F}_{ij}^{\text{D}}$, and $\mathbf{F}_{ij}^{\text{R}}$ are the conservative, dissipative, and random forces, respectively. Furthermore, $\mathbf{r}_{ij} = \mathbf{r}_i - \mathbf{r}_j$, $r_{ij} = \|\mathbf{r}_{ij}\|$, $\mathbf{e}_{ij} = \mathbf{r}_{ij}/r_{ij}$, and $\mathbf{v}_{ij} = \mathbf{v}_i - \mathbf{v}_j$. A white-noise term following the standard normal distribution is denoted by ξ_{ij} . The relations $\xi_{ij} = \xi_{ji}$, $\mathbf{e}_{ij} = -\mathbf{e}_{ji}$, and $\mathbf{v}_{ij} = -\mathbf{v}_{ji}$ guarantee the conservation of momenta. Weight functions are denoted by $\omega^{\text{D}}(r_{ij})$ and $\omega^{\text{R}}(r_{ij})$, whereas γ and σ are constant coefficients. The weight functions and coefficients independently satisfy Einstein's relation⁵ through

$$\begin{aligned}[\omega^{\text{R}}(r_{ij})]^2 &= \omega^{\text{D}}(r_{ij}), \\ \sigma^2 &= 2\gamma k_{\text{B}}T.\end{aligned}\quad (9)$$

C. Simulation details

1. Measurement

The RBC membrane was first equilibrated in the NVT ensemble, i.e., the isothermal condition, by regulating the membrane temperature using a DPD thermostat. After the

membrane reached equilibrium, the thermostat was turned off, and simulations were performed in the NVE ensemble, i.e., the isoenergetic condition. For simulation results in the NVT ensemble, see Appendix C.

The membrane was first thermalized for 1.1 ms (40000 steps) with a DPD thermostat. Then, the thermostat was turned off and the simulation was performed in the NVE ensemble for another 1.1 ms, where the physical quantities were computed. The particle averages of the potentials V_{FENE} , V_{POW} , V_{area} , V_{volume} , and V_{bending} were separately calculated at every step, to which the temporal Fourier transform ($t \rightarrow f = \omega/(2\pi)$) was applied. The Fourier spectra were computed for two different values of the parameters k_s of V_{FENE} , k_p of V_{POW} , k_a of V_{area} , k_v of V_{volume} , and k_b of V_{bending} , that is, the original value and a value set 20% smaller. When a peak shift was observed between the two different values of a parameter, the peak was identified as originating from the corresponding membrane potential. We performed 7000 independent runs for each parameter with different random seeds of the DPD thermostat.

Experiments cannot directly measure the potential energy of the membrane, unlike numerical calculations. Therefore, we also measured the radius of gyration R_α ($\alpha = x, y, z$) as an experimentally measurable quantity. R_α represents the spatial spread of membrane particles along the α -axis and is defined as

$$R_\alpha = \sqrt{\sum_{i=1}^N \frac{\alpha_i^2}{N}}, \quad (10)$$

where N is the number of particles. The Cartesian coordinates of the i th particle ($i = 1, 2, \dots, N$) relative to the center of mass of the RBC are written as (x_i, y_i, z_i) . Optical tweezer experiments can currently measure the RBC membrane displacement with sub-nanometer precision¹⁷. This corresponds to the measurement of the radius of gyration in our simulations.

2. Membrane mass

The mass of the RBC membrane M_{memb} must be explicitly treated in this study as the frequency f of the Fourier spectra is scaled as $f \propto \sqrt{k/M_{\text{memb}}}$, where $k = k_s, k_a, k_v$, or k_b . The mean corpuscular hemoglobin—the total mass of the protein hemoglobin in a single RBC—has been measured to be 28–29 pg^{27,28}. Considering that hemoglobin composes

95–98% of the RBC mass without water, we treat the remaining mass (2–5%) to be that of the RBC membrane. This yields a membrane mass of 0.6–1.5 pg. Here, we take it to be 1.0 pg, which is distributed evenly among the membrane particles.

D. Model parameters

Model parameters and their values are listed below in Table 1 in terms of the model and SI units.

TABLE I: List of model parameters.

parameter	symbol	value (model units)	value (SI units)
number of steps	—	80000	80000
time-step size	—	0.005	28 ns
cutoff radius	—	12.2	3.13 μm
damping coefficient	γ	0.05	18 pg/s
temperature	$k_{\text{B}}T$	1	4.14×10^{-21} J
particle mass	m	1	2 fg
number of particles	N	492	492
RBC diameter	D_0	30.5	7.82 μm
—	a_0	0.0518	0.0518
—	a_1	2.0026	2.0026
—	a_2	−4.491	−4.491
coefficient of V_{FENE}	k_{s}	48.6	3.06 $\mu\text{N/m}$
coefficient of V_{area}	k_{a}	5000	315 $\mu\text{N/m}$
coefficient of V_{volume}	k_{v}	5000	1.23 kPa
coefficient of V_{bending}	k_{b}	66.9	2.77×10^{-19} J
spring eq. length vs max. length	x_0	0.488	0.488

III. RESULTS

A. Time evolution of energies

The time evolutions of the average total energy and the total potential energy V_{RBC} per particle are shown in Figs. 2 (a) and (b), respectively. We applied the DPD thermostat for the first 1.1 ms, where the relaxation time τ calculated from an exponential fit is 0.02 ms. We then continued the simulation for another 1.1 ms with the thermostat turned off. Reflecting this condition, the total energy was conserved in the second half of the simulation. On the other hand, the potential energy continued to fluctuate.

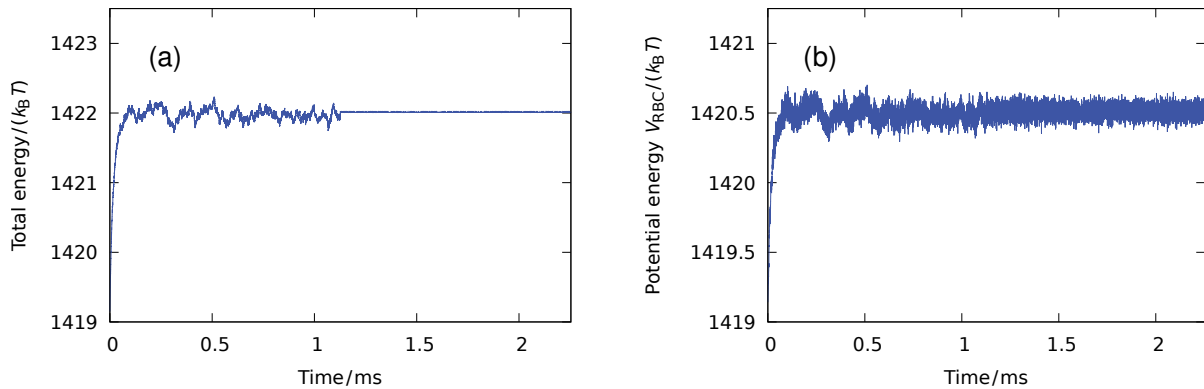


FIG. 2: Effect of the DPD thermostat in terms of the time evolutions of (a) the total energy and (b) the total potential energy V_{RBC} . The thermostat was turned off 1.1 ms into the simulation, at which point the simulation switched to NVE. As a result, the total energy was conserved, whereas the potential energy continued to fluctuate.

B. Spectra of potential energies

1. Spectra and characteristic peaks

As given by Eq. (2), the potential energy V_{RBC} is the sum of four different potentials, namely, V_{FENE} , V_{area} , V_{volume} , and V_{bending} . The Fourier spectra of these potentials are shown in Figs. 3 (a), (b), (c), and (d), respectively. The results of V_{FENE} will represent the results of V_{POW} and V_{spring} because the spectrum of V_{POW} was found to be identical to that of

V_{FENE} , and V_{spring} is simply the sum of V_{FENE} and V_{POW} . Distinct peaks appear in each spectrum, several of which are observed in many figures. Hence, we named four peaks at different frequencies as identified in the figures as follows: p_{s1} at 62 kHz, p_{s2} at 200 kHz, p_{v1} at 2.6 MHz, and p_{v2} at 5.2 MHz. In Fig. 3 (a) for V_{FENE} , the peaks p_{s1} , p_{s2} , and p_{v1} appear, whereas in Fig. 3 (b) for V_{area} , the peaks p_{s1} , p_{v1} , and p_{v2} are observed. All four peaks are visible in Fig. 3 (c) for V_{volume} , whereas the peaks p_{s1} and p_{v1} are seen in Fig. 3 (d) for V_{bending} .

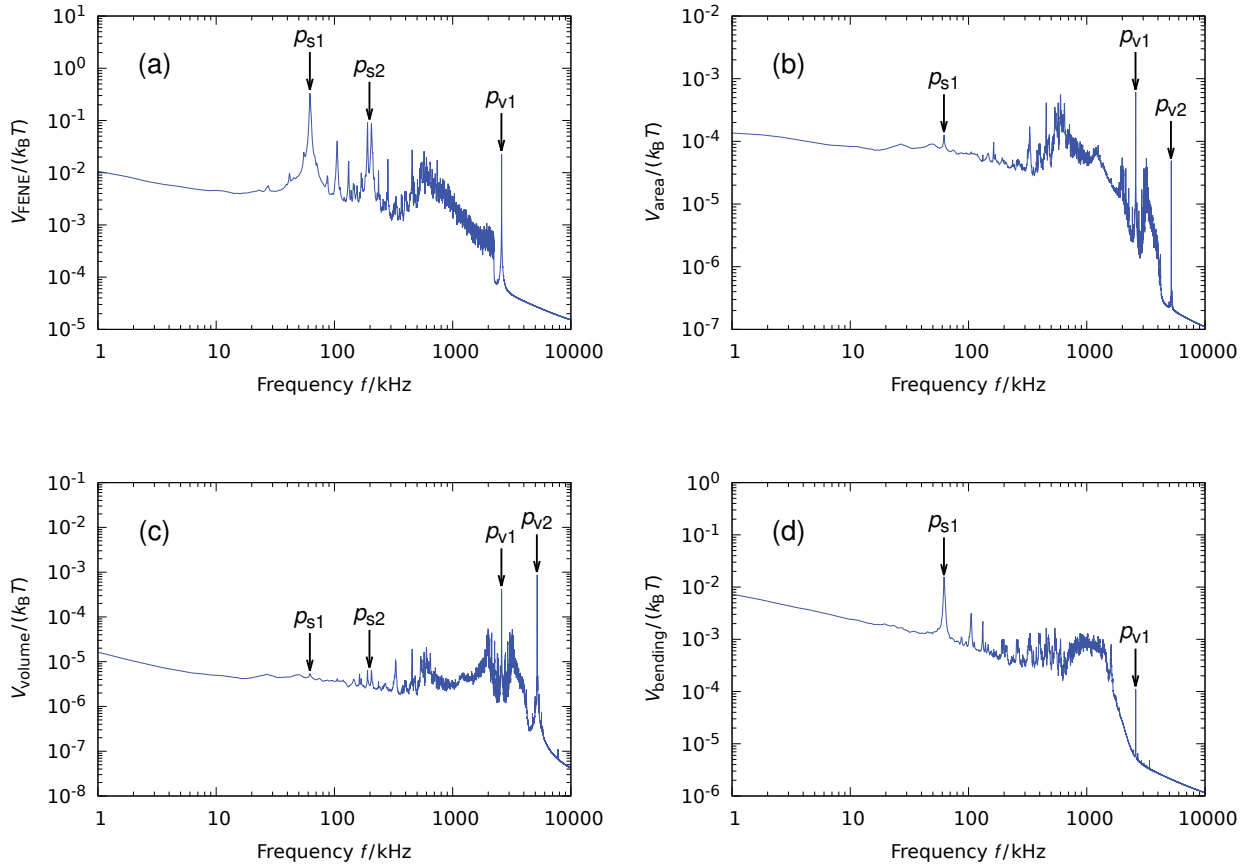


FIG. 3: Fourier spectra of fluctuations of membrane potentials: (a) V_{FENE} , (b) V_{area} , (c) V_{volume} , and (d) V_{bending} . The peak p_{s1} is at 62 kHz, p_{s2} at 200 kHz, p_{v1} at 2.6 MHz, and p_{v2} at 5.2 MHz. Each peak is observed in more than one spectrum.

2. *Parameter dependence of spectra*

We hypothesized that the peaks observed in many spectra at identical frequencies originated from the same potential. To identify the origin of each peak, we performed another set of simulations. The values of the parameters k_s of V_{FENE} , k_a of V_{area} , k_v of V_{volume} , and k_b of V_{bending} were reduced by 20% from their original values. The results are shown in Fig. 4, where the newly obtained spectra (dashed line) are superimposed on the original spectra of Fig. 3 (solid line). As in Fig. 3, the spectra of V_{FENE} , V_{area} , V_{volume} , and V_{bending} are labeled (a), (b), (c), and (d), respectively. Altering the values of the parameters resulted in an overall shift in all the spectra. However, the peaks p_{s1} and p_{s2} have shifted only in Fig. 4 (a) for V_{FENE} , whereas Fig. 4 (c) for V_{volume} is the only figure in which p_{v1} and p_{v2} are seen to shift. Moreover, no distinct peak shifts are observed in Fig. 4 (b) for V_{area} and Fig. 4 (d) for V_{bending} . This implies that all the characteristic peaks identifiable in the Fourier spectra of membrane potentials originate from V_{FENE} and V_{volume} .

C. *Spectra of the radius of gyration*

Although we have thus far identified the peaks observed in the Fourier spectra of the membrane potentials, the potentials themselves are not directly measurable by experiments. Accordingly, we measured the radii of gyration R_x , R_y , and R_z given by Eq. (10). Considering the rotational symmetry of the RBC in the xy -plane, the spectra of R_x are shown in Fig. 5, whereas the spectra of R_z are shown in Fig. 6. In both figures, the parameters k_s of V_{FENE} , k_a of V_{area} , k_v of V_{volume} , and k_b of V_{bending} are altered in (a), (b), (c), and (d), respectively. The peak p_{s1} has a frequency of 62 kHz and p_{v1} has a frequency of 2.6 MHz, identical to the peaks in Figs. 3 and 4. In both the spectra of R_x and R_z , no peak shifts are observed in (b) and (d), where the corresponding parameters of V_{area} and V_{bending} were altered. On the other hand, the dependence of p_{s1} on V_{FENE} is seen in (a), as is the dependence of p_{v1} on V_{volume} in (c). Although Figs. 5 and 6 show similar results, an important distinction should be made regarding p_{s1} . The peak is surrounded by other similar peaks in Fig. 5, whereas it is independent of other peaks in Fig. 6. This implies that p_{s1} is more easily observed in the spectrum of R_z .

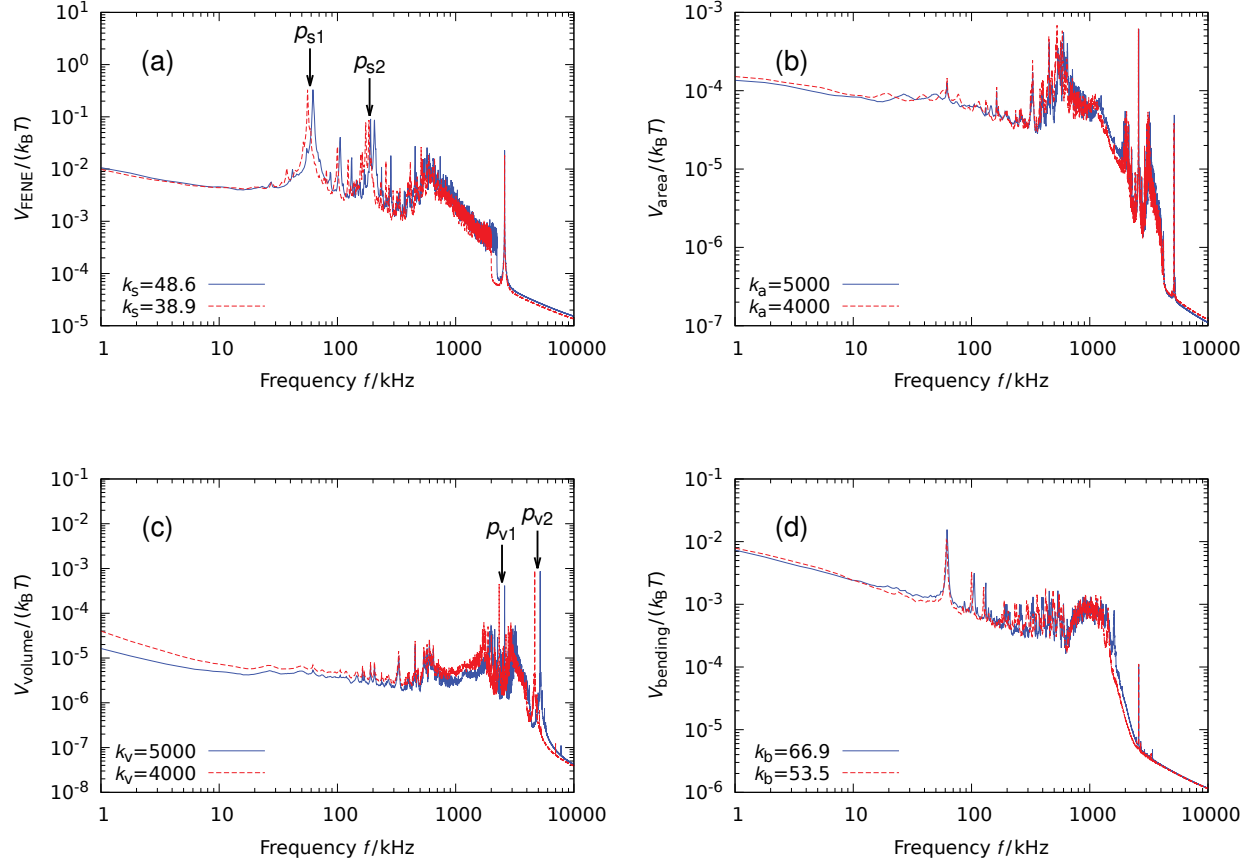


FIG. 4: (Color online) Fourier spectra of fluctuations of membrane potentials: (a) V_{FENE} , (b) V_{area} , (c) V_{volume} , and (d) V_{bending} . The original spectra shown in Fig. 3 are represented as solid lines, and the dashed lines are the new spectra where the values of the parameters k_s , k_a , k_v , and k_b were altered. The peak shifts of p_{s1} and p_{s2} are observed only in (a) for V_{FENE} , whereas the peak shifts of p_{v1} and p_{v2} are only seen in (c) for V_{volume} .

D. Feasibility in experiments

Experiments have been conducted where they measured the Fourier spectra of the membrane fluctuations of an RBC^{17,29}. However, the results of these experiments cannot be directly compared with our results due to several differences in the environment and methods of measurement. First, in experiments, the RBCs are placed in a saline solution, whereas our simulations are performed in a vacuum. Second, the observable in experiments is the position of the rim of the membrane or the attached beads, whereas the radius of gyration is

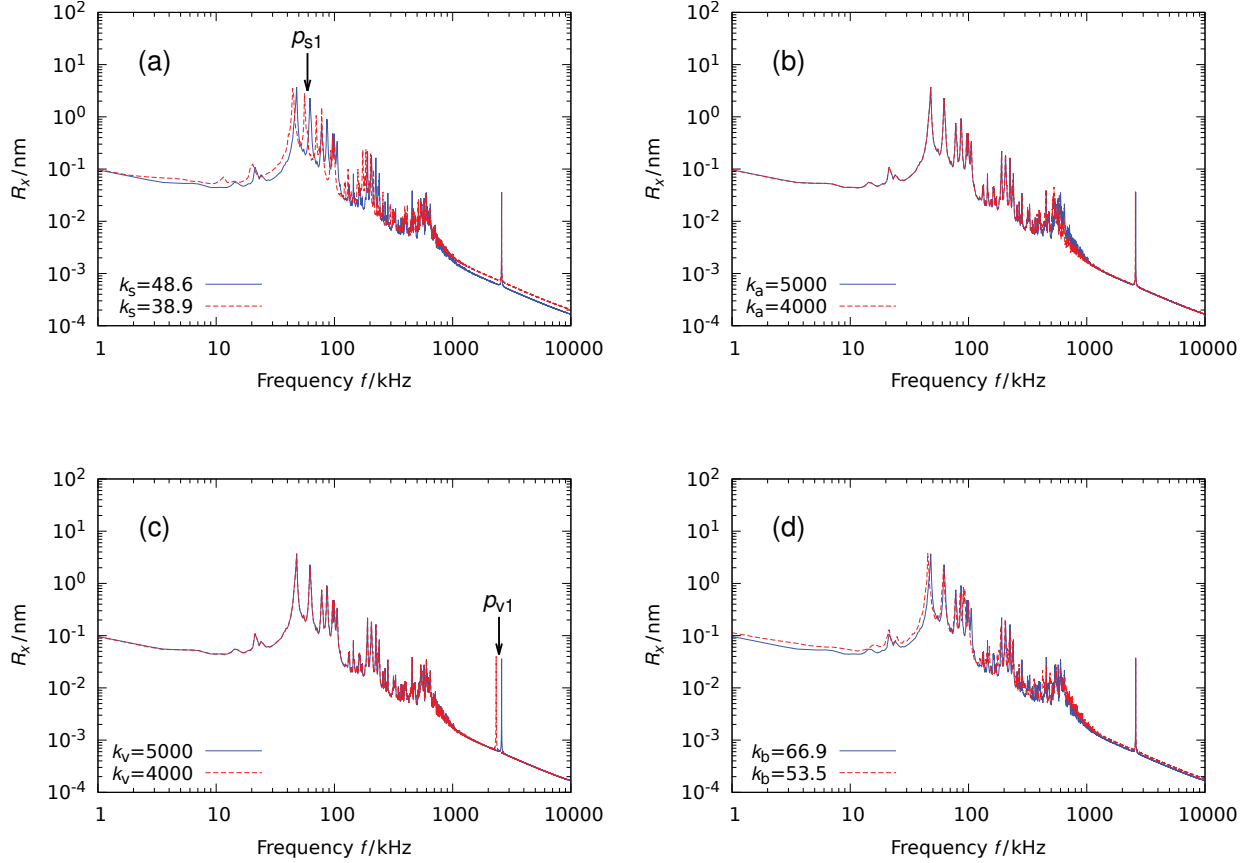


FIG. 5: (Color online) Fourier spectra of the radius of gyration R_x . The parameters k_s , k_a , k_v , and k_b were each altered in their corresponding figures in (a), (b), (c), and (d). The peak p_{s1} has a frequency of 62 kHz and p_{v1} a frequency of 2.6 MHz.

measured in our simulations. Third, only the frequencies up to approximately 100 Hz were measured in the previously mentioned experiments, which is below the frequency range of the peaks intrinsic to the RBC membrane as measured in our simulations. Therefore, in the following, we discuss the feasibility of our simulations in experiments regarding these three problems.

1. *Viscosity of the surrounding fluids*

To consider the effect of the surrounding fluids, we performed a set of simulations using the Langevin thermostat instead of the DPD thermostat to implicitly simulate the interactions between the membrane and the surrounding fluids. The Langevin thermostat is reflected in

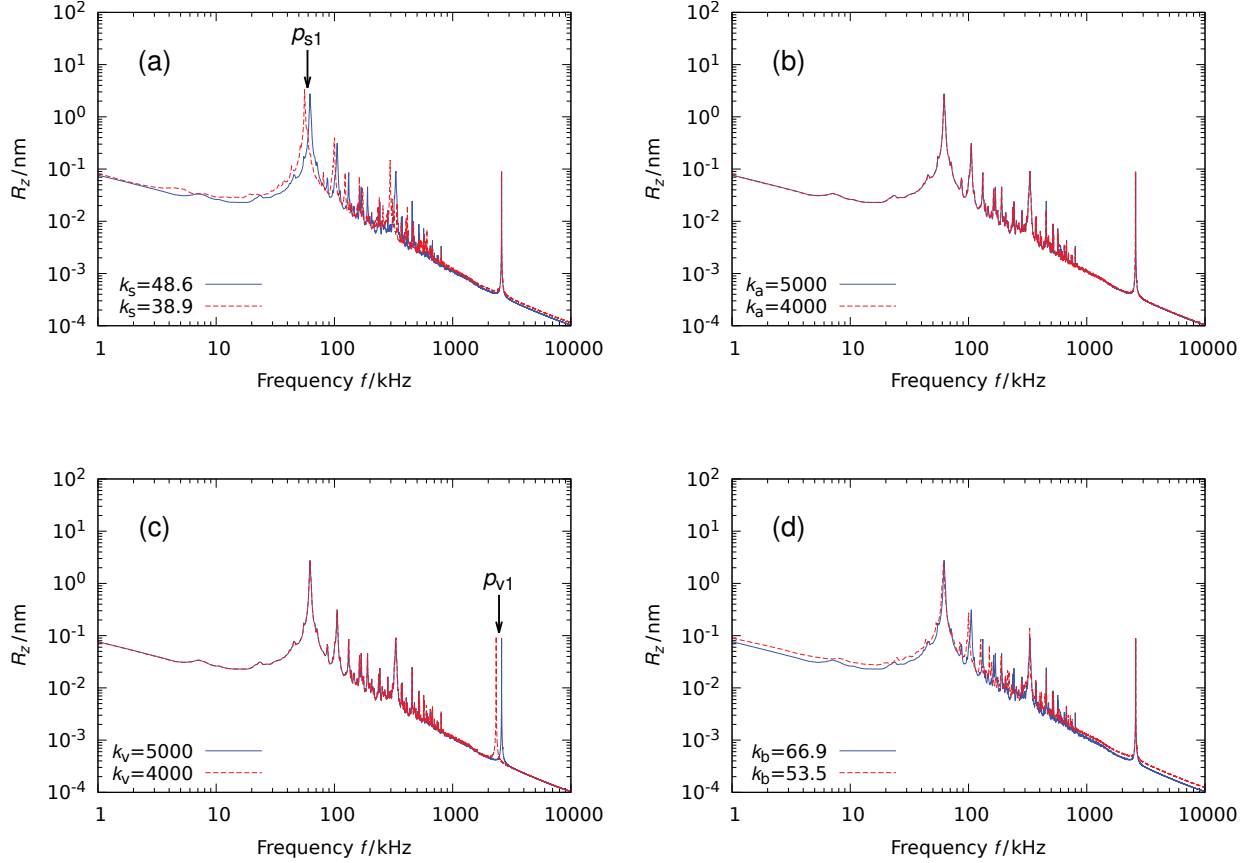


FIG. 6: (Color online) Fourier spectra of the radius of gyration R_z . The parameters k_s , k_a , k_v , and k_b were each altered in their corresponding figures in (a), (b), (c), and (d). The peak p_{s1} has a frequency of 62 kHz and p_{v1} a frequency of 2.6 MHz.

the equation of motion for a single particle, which is expressed as

$$m\dot{\mathbf{v}} = \mathbf{F}^C - \lambda\mathbf{v} + \sqrt{2\lambda k_B T}\mathbf{R}. \quad (11)$$

Here, \mathbf{F}^C is the conservative force, λ is the damping coefficient, and the force \mathbf{R} is a Gaussian white noise satisfying

$$\langle \mathbf{R}(t) \rangle = \mathbf{0}, \quad (12)$$

$$\langle \mathbf{R}(t) \cdot \mathbf{R}(t') \rangle = \delta(t - t'). \quad (13)$$

The strength of the thermostat and its effect on the membrane fluctuations are determined by λ given a constant temperature T . However, we are currently unaware of the value of λ for the Langevin thermostat corresponding to the cytoplasm and the suspending fluid in

an experimental setting. Therefore, we performed simulations for different values of λ and investigated the effect of λ on the Fourier spectra. Considering a realistic sample size for experiments, the spectra were averaged over 100 samples for each value of λ .

Figure 7 shows the spectra of the radius of gyration R_z for different values of the damping coefficient λ introduced in Eq. (11). The peaks p_{s1} and p_{v1} are detectable for both $\lambda = 0.02$ and 0.2 , meaning that a sample size of 100 is sufficient to detect the larger peaks. The two spectra are different in that the spectrum for the larger value of $\lambda = 0.2$ is smoother with broader peaks. This implies that the peaks will be less pronounced as the viscosity of the surrounding fluids increases. Because we currently do not know the physical value of λ , the peaks may not be experimentally observable due to considerable thermal noise. In that case, alternative measurements must be conducted, such as by taking the correlation of fluctuations at two points to cancel out the noise.

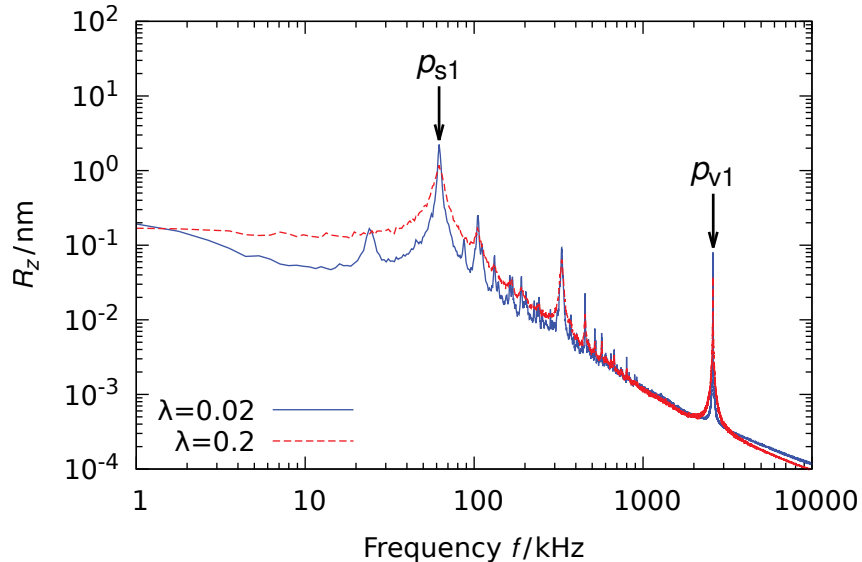


FIG. 7: (Color online) Fourier spectra of the radius of gyration R_z for $\lambda = 0.02$ and 0.2 , where λ is the damping coefficient introduced in Eq. (11). The peak p_{s1} has a frequency of

62 kHz and p_{v1} a frequency of 2.6 MHz.

2. Comparison of point fluctuations and the radius of gyration

We measured the fluctuations of single points on the membrane in addition to the radius of gyration to investigate the differences between the observables. The locations of the

observed points are shown in Fig. 8, each composed of 7 membrane particles. We chose three locations at the middle (M), upper (U), and lower (L) points along the equator as shown in Fig. 8 (a). We chose another four locations at the east (E), west (W), north (N), and south (S) points at the top as shown in Fig. 8 (b). Points on the equator were measured for the fluctuations in the x -axis direction, whereas those at the top were measured for the fluctuations in the z -axis direction. We compared the resulting spectra with those of the radii of gyration R_x and R_z . The sample size was kept at 100 for the measurements.

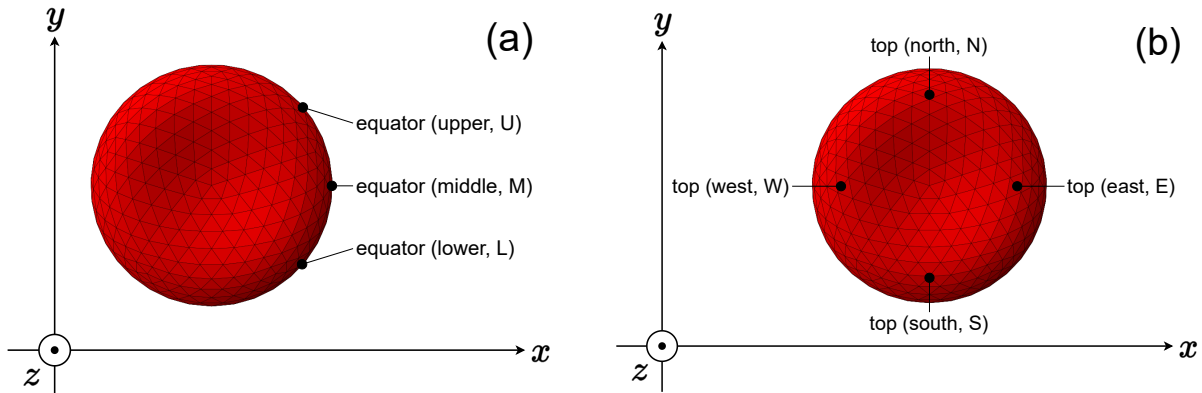


FIG. 8: (Color online) Single points where the membrane fluctuations are measured. Measurement in the (a) x -axis and (b) z -axis directions.

The comparison between the spectra of point fluctuations and the radii of gyration R_x and R_z are shown in Fig. 9 for the damping constant $\lambda = 0.2$. The spectra of the fluctuations of particles at the RBC equator are shown in Fig. 9 (a). The notation (MUL) denotes the average of the fluctuations for the three points. Figure 9 (b) shows the spectra of the fluctuations of particles at the top. The notation (EWNS) similarly denotes the average of the fluctuations. In Fig. 9 (a), the peaks p_{s1} and p_{v1} are observable for all three spectra. However, in Fig. 9 (b), the peak p_{s1} is not observed for the fluctuations at the top (E) unlike the fluctuations at the top (EWNS) and R_z . This suggests that averaging the membrane fluctuations either over several points or the entire membrane improves the observability of the peaks for fluctuations in the z -axis direction.

Although the spectra of the averaged point fluctuations are comparable to those of the radii of gyration, the latter exhibits more distinct peaks in certain frequencies. It should be possible in principle to average the membrane fluctuations over an entire surface (e.g. the top

surface as seen in Fig. 8) similar to the radius of gyration using image analysis techniques. Image analysis has already been employed to measure RBC membrane fluctuations at the rim³⁰. The extension of such methods to the measurement over an entire surface should be considered for future experiments.

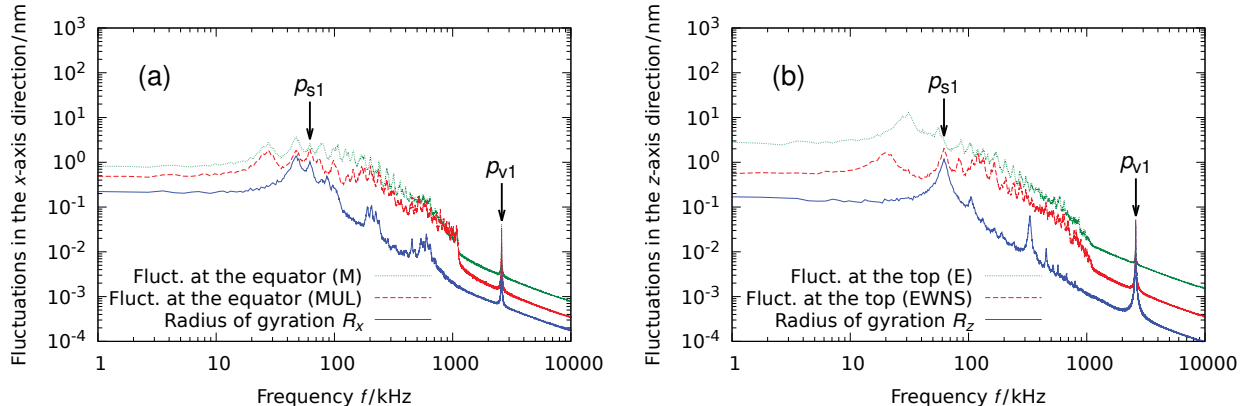


FIG. 9: (Color online) Fourier spectra of the point fluctuations and the radii of gyration R_x and R_z for $\lambda = 0.2$. (a) Spectra of fluctuations in the x -axis direction. R_x is compared with fluctuations at the middle (M), upper (U), and lower (L) points along the equator. (b) Spectra of fluctuations in the z -axis direction. R_z is compared with fluctuations at the east (E), west (W), north (N), and south (S) points at the top. The notations (MUL) and (EWNS) denote the average fluctuations of their respective points.

3. Range of measurable frequencies

The maximum frequency for the experimentally measured Fourier spectra of RBC membrane fluctuations is approximately 100 Hz^{17,29}. However, the experimental setup proposed by Gögler *et al.* allows us to measure membrane fluctuations up to 200 kHz¹⁷. Additionally, this maximum frequency is limited only by the bandwidth of the bus connecting the experimental device and the computer. Measurement at higher frequencies around 1 MHz would be feasible for higher-performance buses. In this case, all the peaks found in the present manuscript would be within the range of observable frequencies. Even for the current frequency range capped at 200 kHz, the peak p_{s1} at 62 kHz is observable. As discussed in the next section, p_{s1} is the most important signal. Therefore, measuring p_{s1} alone would be

meaningful.

IV. SUMMARY AND DISCUSSION

In this study, we developed a method of precisely determining the parameter values used in a DPD model of the RBC by focusing on the fluctuations of the RBC membrane. We measured the Fourier spectra of the FENE potential V_{FENE} , the area-conserving potential V_{area} , the volume-conserving potential V_{volume} , and the bending potential V_{bending} . Several distinct peaks were observed across multiple spectra. The peaks p_{s1} (62 kHz) and p_{s2} (200 kHz) were determined to be from V_{FENE} , whereas the peaks p_{v1} (2.6 MHz) and p_{v2} (5.2 MHz) were found to originate from V_{volume} .

We further measured the Fourier spectra of the radius of gyration and compared them to the spectra obtained from point fluctuations. The spectra of both measurements exhibited the characteristic peaks p_{s1} and p_{v1} , which reinforces the experimental feasibility of our simulations. The same comparison also suggests that the peaks are better detected for the average of membrane fluctuations at different points than the fluctuations at a single point. We also observed that the peak p_{s1} exhibited a singular peak when measured in the z -axis direction, making it more detectable than in the x -axis direction. We attribute this discrepancy to the anisotropic nature of the RBC membrane, although further studies are necessary to rule out numerical artifacts.

Theoretically, these results enable us to determine the values of the parameters k_s and k_v corresponding to their respective peaks p_{s1} and p_{v1} . In actuality, however, the value of k_v is limited by the time-step size of the simulation, and that of a physical RBC is much larger than is numerically feasible owing to its highly incompressible nature. On the other hand, the parameter k_s is determined from the shear modulus of the membrane alone. Therefore, we can determine the value of k_s by measuring the frequency of p_{s1} experimentally.

We believe that the coarse-grained nature of the RBC model used in our simulations exhibits universality to some extent. The potentials V_{area} , V_{volume} , and V_{bending} used in the model reflect the lower-order contributions of the incompressibility and bending energy of the membrane. This means that the equations of these potentials leave little room for alternative formulations. This is not the case for the spring potential V_{spring} , for which there are multiple appropriate equations. However, regardless of the model equation used, V_{spring}

can be fundamentally expressed as a quadratic mass-spring-damper (MSD) system around small deviations from equilibrium. In this case, the peak frequencies of the Fourier spectra are determined by the oscillation frequency of the MSD system, irrespective of the details of the spring potential. Note that the inaccuracy of the coarse-grained approximation of the membrane potentials becomes more prominent when the membrane is far from equilibrium such as under large deformations or strong flows^{31,32}. Therefore, the scope of the proposed methods is limited to measuring the membrane fluctuations close to equilibrium.

In this study, we considered the lowest oscillation mode of membrane fluctuations. Concurrent measurement in multiple directions will enable us to associate the model parameters with oscillation modes of higher degrees. On the other hand, the membrane fluctuations of an RBC are known to violate the fluctuation–dissipation relation, which suggests the presence of non-equilibrium processes^{16,18}. The methods proposed in the present paper can be applied to investigating the non-equilibrium behavior of RBCs. Measuring the Fourier spectra of the membrane energies and fluctuations will enable us to quantify the dissipation of energy induced by non-equilibrium contributions.

ACKNOWLEDGMENTS

The authors would like to thank H. Noguchi and H. Nakano for fruitful discussions. This research was supported by JSPS KAKENHI, Grant No. JP21K11923. The computation was partly carried out using the facilities of the Supercomputer Center, Institute for Solid State Physics (ISSP), University of Tokyo.

Appendix A: Dependence of peak frequencies on coarse graining

The outermost layer of a physical RBC is a lipid bilayer with the cytoskeleton attached underneath³³. The lipid bilayer is continuous in the length scale of an RBC, whereas the cytoskeleton is estimated to contain approximately 27000–45000 actin nodes¹⁵. This is on the basis of a node density of 200–330/ μm^2 , with 135 μm^2 adopted as the average surface area^{34,35}. On the other hand, the actin nodes are coarse-grained using 492 particles in this study, which is considerably less than the actual values. Therefore, we must investigate how the coarse graining affects the peak frequencies of the Fourier spectra. We performed

a simulation varying the number of particles used to discretize the RBC. We measured the frequencies of the aforementioned peaks p_{s1} of V_{FENE} and p_{v1} of V_{volume} with the number of particles $N = 162, 252, 362, 492,$ and 1002 . The same values of the model parameters $k_s, k_a, k_v,$ and k_b were used in each case, independent of N . On the other hand, the particle mass was adjusted to keep the membrane mass constant.

As shown in Fig. 10, the peak frequencies of p_{s1} and p_{v1} exhibit virtually no dependence on the number of particles. The plot points were fit to $f(N) = f(\infty) + a/N$, where $f(N)$ denotes the peak frequency. By comparing the peak frequencies at $N \rightarrow \infty$ (the continuum limit) and $N = 492$ (the number of particles used in the simulations), we found that the difference between $f(\infty)$ and $f(492)$ was within 1% in both Figs. 10 (a) and (b). Therefore, the dependence of peak frequencies on coarse graining is negligible for the peaks of both V_{FENE} and V_{volume} .

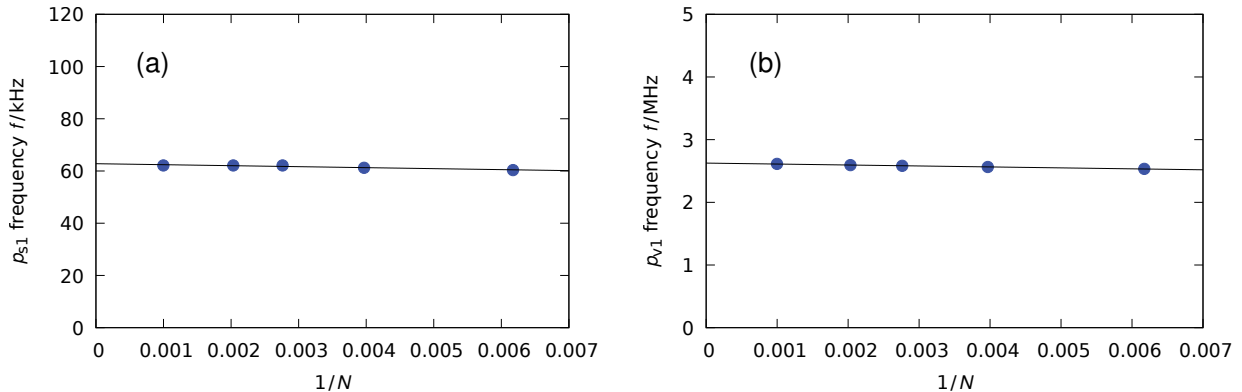


FIG. 10: Peak frequencies plotted against $1/N$, where N is the number of particles: (a) p_{s1} and (b) p_{v1} . Plot points are fit to $f(N) = f(\infty) + a/N$, where $f(N)$ denotes the peak frequency.

Appendix B: Equations of membrane forces

The nodal forces corresponding to the membrane potentials $V_{\text{spring}}, V_{\text{area}}, V_{\text{volume}},$ and V_{bending} will be explained below. Definitions and notations are mostly identical to those in the previous work by Fedosov³⁶.

1. Spring forces from V_{spring}

The force $\mathbf{F}_{ij}^{\text{spring}}$ corresponding to Eq. (3) is a force that the j th particle exerts on the neighboring i th particle along the side of a triangular lattice:

$$\mathbf{F}_{ij}^{\text{spring}} = \left(-\frac{k_s l_{ij}}{1-x^2} + \frac{k_p}{l_{ij}^2} \right) \hat{\mathbf{l}}_{ij}. \quad (\text{B1})$$

Here, l_{ij} is the length of the spring and $x = l_{ij}/l_{ij}^m$, where l_{ij}^m is the maximum length of the spring. Additionally, $\hat{\mathbf{l}}_{ij} = \mathbf{l}_{ij}/l_{ij}$ is a unit vector between the two ends of the spring.

2. Area- and volume-conserving forces from V_{area} and V_{volume}

Suppose we take a single triangular lattice comprising the RBC membrane, as shown in Fig. 11. The vector extending from the j th particle to the i th particle is denoted by $\mathbf{a}_{ij} = \mathbf{p}_i - \mathbf{p}_j$, where $i, j = 1, 2, 3$. Furthermore, the normal vector $\boldsymbol{\xi} = \mathbf{a}_{21} \times \mathbf{a}_{31}$ is taken such that it always points outward away from the membrane. The area A_t and the volume V_t occupied by the current lattice at time t are expressed as $A_t = \|\boldsymbol{\xi}\|/2$ and $V_t = \boldsymbol{\xi} \cdot \mathbf{r}_c/6$. Here, $\mathbf{r}_c = (\mathbf{p}_1 + \mathbf{p}_2 + \mathbf{p}_3)/3$ is the center of mass of the lattice relative to that of the entire membrane. Given these definitions, consider the following coefficients β_a and β_v :

$$\beta_a = -k_a \frac{A_t^{\text{tot}} - A_0^{\text{tot}}}{A_0^{\text{tot}}}, \quad \beta_v = -k_v \frac{V_t^{\text{tot}} - V_0^{\text{tot}}}{V_0^{\text{tot}}}, \quad (\text{B2})$$

where A_t^{tot} and A_0^{tot} are the current and initial total membrane areas, respectively, with an analogous notation for the volumes V_t^{tot} and V_0^{tot} . Using β_a and β_v , we can write the forces $\mathbf{F}_i^{\text{area}}$ and $\mathbf{F}_i^{\text{volume}}$ acting on the i th ($i = 1, 2, 3$) particle of the triangular lattice as

$$\mathbf{F}_1^{\text{area}} = \frac{\beta_a}{4A_t} (\boldsymbol{\xi} \times \mathbf{a}_{32}), \quad \mathbf{F}_1^{\text{volume}} = \frac{\beta_v}{6} \left(\frac{\boldsymbol{\xi}}{3} + \mathbf{r}_c \times \mathbf{a}_{32} \right), \quad (\text{B3})$$

$$\mathbf{F}_2^{\text{area}} = \frac{\beta_a}{4A_t} (\boldsymbol{\xi} \times \mathbf{a}_{13}), \quad \mathbf{F}_2^{\text{volume}} = \frac{\beta_v}{6} \left(\frac{\boldsymbol{\xi}}{3} + \mathbf{r}_c \times \mathbf{a}_{13} \right), \quad (\text{B4})$$

$$\mathbf{F}_3^{\text{area}} = \frac{\beta_a}{4A_t} (\boldsymbol{\xi} \times \mathbf{a}_{21}), \quad \mathbf{F}_3^{\text{volume}} = \frac{\beta_v}{6} \left(\frac{\boldsymbol{\xi}}{3} + \mathbf{r}_c \times \mathbf{a}_{21} \right), \quad (\text{B5})$$

where $\mathbf{F}_i^{\text{area}}$ and $\mathbf{F}_i^{\text{volume}}$ correspond to Eqs. (4) and (5), respectively.

3. Bending forces from V_{bending}

Shown in Fig. 12 are two adjacent triangular lattices, where the normal vectors $\boldsymbol{\xi} = \mathbf{a}_{21} \times \mathbf{a}_{31}$ and $\boldsymbol{\zeta} = \mathbf{a}_{34} \times \mathbf{a}_{24}$. If $(\boldsymbol{\xi} - \boldsymbol{\zeta}) \cdot (\mathbf{r}_c^\xi - \mathbf{r}_c^\zeta) < 0$, where \mathbf{r}_c^ξ and \mathbf{r}_c^ζ are the centers of

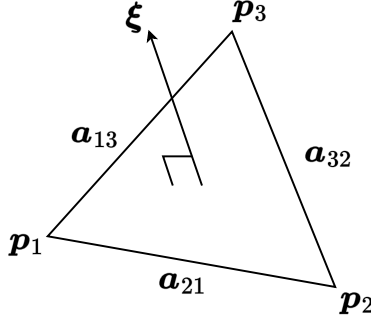


FIG. 11: Illustration of a triangular lattice comprising the RBC membrane. p_i represents a vertex and a_{ij} denotes a side, where $i, j = 1, 2, 3$. ξ is a normal vector always taken to point outward from the membrane.

mass of the respective lattices, then the labels p_2 and p_3 are swapped, after which the sides and normal vectors are recalculated. The dihedral angle θ is written as

$$\theta = \cos^{-1} \left(\frac{\xi}{\|\xi\|} \cdot \frac{\zeta}{\|\zeta\|} \right), \quad (\text{B6})$$

which is equal to the angle between ξ and ζ . We then define three coefficients,

$$b_{11} = -\frac{\beta_b \cos \theta}{\|\xi\|^2}, \quad b_{12} = \frac{\beta_b}{\|\xi\| \|\zeta\|}, \quad b_{22} = -\frac{\beta_b \cos \theta}{\|\zeta\|^2}, \quad (\text{B7})$$

where $\beta_b = k_b \sin(\theta - \theta_0) / \sqrt{1 - \cos^2 \theta}$, with θ_0 being the spontaneous angle. These definitions provide a force $\mathbf{F}_i^{\text{bending}}$ corresponding to Eq. (6), exerted on the i th particle ($i = 1, 2, 3, 4$) of the two adjacent triangular lattices:

$$\mathbf{F}_1^{\text{bending}} = b_{11} (\xi \times \mathbf{a}_{32}) + b_{12} (\zeta \times \mathbf{a}_{32}), \quad (\text{B8})$$

$$\mathbf{F}_2^{\text{bending}} = b_{11} (\xi \times \mathbf{a}_{13}) + b_{12} (\xi \times \mathbf{a}_{34} + \zeta \times \mathbf{a}_{13}) + b_{22} (\zeta \times \mathbf{a}_{34}), \quad (\text{B9})$$

$$\mathbf{F}_3^{\text{bending}} = b_{11} (\xi \times \mathbf{a}_{21}) + b_{12} (\xi \times \mathbf{a}_{42} + \zeta \times \mathbf{a}_{21}) + b_{22} (\zeta \times \mathbf{a}_{42}), \quad (\text{B10})$$

$$\mathbf{F}_4^{\text{bending}} = b_{12} (\xi \times \mathbf{a}_{23}) + b_{22} (\zeta \times \mathbf{a}_{23}). \quad (\text{B11})$$

Appendix C: Spectra in the NVT ensemble

The Fourier spectra listed in Sec. III of this paper were obtained from an NVE simulation where the DPD thermostat was turned off after the membrane reached the equilibrium. As

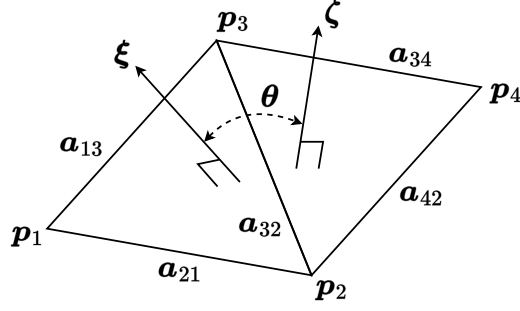


FIG. 12: Illustration of two adjacent triangular lattices taken from the RBC membrane. p_i represents a vertex and a_{ij} denotes a side, where $i, j = 1, 2, 3, 4$. ξ and ζ are normal vectors, whereas θ is the dihedral angle equal to the angle between ξ and ζ .

a comparison, Fig. 13 shows in dashed lines the spectra of V_{FENE} and V_{volume} from an NVT simulation where the thermostat was applied throughout. The corresponding spectra from the NVE simulation are shown in solid lines. The two spectra differ in that the NVT spectra have a less pronounced profile, have wider peaks, and show a bias at lower frequencies. Crucially, however, all peak frequencies remain unchanged between NVT and NVE. Therefore, we opted to measure the Fourier spectra in NVE to study the spectra and their peaks in more detail.

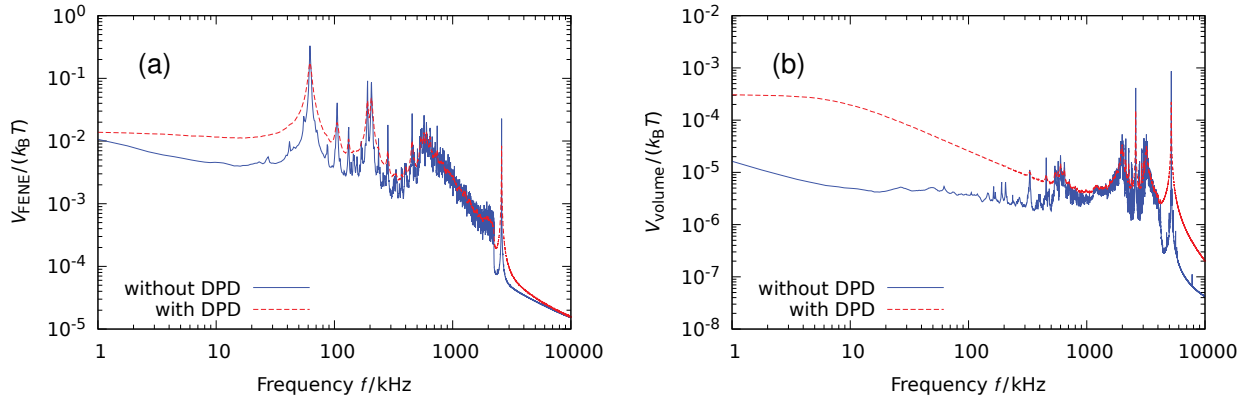


FIG. 13: (Color online) Fourier spectra of fluctuations of membrane potentials: (a) V_{FENE} and (b) V_{volume} . The spectra in dashed lines are those of an NVT simulation, and they are superimposed on the solid spectra of the NVE simulation discussed in Sec. III.

REFERENCES

- ¹J. Shi, P. W. Kantoff, R. Wooster, and O. C. Farokhzad, “Cancer nanomedicine: progress, challenges and opportunities,” *Nat. Rev. Cancer* **17**, 20–37 (2017).
- ²S.-C. Liu, L. H. Derick, S. Zhai, and J. Palek, “Uncoupling of the spectrin-based skeleton from the lipid bilayer in sickled red cells,” *Science* **252**, 574–576 (1991).
- ³Y. Park, M. Diez-Silva, G. Popescu, G. Lykotrafitis, W. Choi, M. S. Feld, and S. Suresh, “Refractive index maps and membrane dynamics of human red blood cells parasitized by *Plasmodium falciparum*,” *PNAS* **105**, 13730–13735 (2008).
- ⁴P. J. Hoogerbrugge and J. M. V. A. Koelman, “Simulating microscopic hydrodynamic phenomena with dissipative particle dynamics,” *EPL* **19**, 155 (1992).
- ⁵P. Español and P. Warren, “Statistical mechanics of dissipative particle dynamics,” *EPL* **30**, 191–196 (1995).
- ⁶G. R. McNamara and G. Zanetti, “Use of the Boltzmann equation to simulate lattice-gas automata,” *Phys. Rev. Lett.* **61**, 2332–2335 (1988).
- ⁷A. Malevanets and R. Kapral, “Mesoscopic model for solvent dynamics,” *J. Chem. Phys.* **110**, 8605–8613 (1999).
- ⁸H. Takeda, S. M. Miyama, and M. Sekiya, “Numerical simulation of viscous flow by smoothed particle hydrodynamics,” *Prog. Theor. Phys.* **92**, 939–960 (1994).
- ⁹D. A. Fedosov, H. Noguchi, and G. Gompper, “Multiscale modeling of blood flow: from single cells to blood rheology,” *BMMB* **13**, 239–258 (2014).
- ¹⁰T. Ye, N. Phan-Thien, and C. T. Lim, “Particle-based simulations of red blood cells—a review,” *J. Biomech.* **49**, 2255–2266 (2016), selected Articles from the International Conference on CFD in Medicine and Biology (Albufeira, Portugal – August 30th – September 4th, 2015).
- ¹¹G. Lenormand, S. Hénon, A. Richert, J. Siméon, and F. Gallet, “Direct measurement of the area expansion and shear moduli of the human red blood cell membrane skeleton,” *Biophys. J.* **81**, 43–56 (2001).
- ¹²L. Scheffer, A. Bitler, E. Ben-Jacob, and R. Korenstein, “Atomic force pulling: probing the local elasticity of the cell membrane,” *Eur. Biophys. J.* **30**, 83–90 (2001).
- ¹³N. Mohandas and E. Evans, “Mechanical properties of the red cell membrane in relation to molecular structure and genetic defects,” *Annu. Rev. Bioph. Biom.* **23**, 787–818 (1994).

- ¹⁴K. Matthews, E. S. Lamoureux, M.-E. Myrand-Lapierre, S. P. Duffy, and H. Ma, “Technologies for measuring red blood cell deformability,” *Lab Chip* **22**, 1254–1274 (2022).
- ¹⁵D. A. Fedosov, B. Caswell, and G. E. Karniadakis, “Systematic coarse-graining of spectrin-level red blood cell models,” *Comput. Methods Appl. Mech. Eng.* **199**, 1937–1948 (2010).
- ¹⁶F. S. Gnesotto, F. Mura, J. Gladrow, and C. P. Broedersz, “Broken detailed balance and non-equilibrium dynamics in living systems: a review,” *Rep. Prog. Phys.* **81**, 066601 (2018).
- ¹⁷M. Gögler, T. Betz, and J. A. Käs, “Simultaneous manipulation and detection of living cell membrane dynamics,” *Opt. Lett.* **32**, 1893–1895 (2007).
- ¹⁸H. Turlier, D. A. Fedosov, B. Audoly, T. Auth, N. S. Gov, C. Sykes, J.-F. Joanny, G. Gompper, and T. Betz, “Equilibrium physics breakdown reveals the active nature of red blood cell flickering,” *Nat. Phys.* **12**, 513–519 (2016).
- ¹⁹Y. C. Fung, W. C. Tsang, and P. Patitucci, “High-resolution data on the geometry of red blood cells,” *Biorheology* **18**, 369–385 (1981), 3-6.
- ²⁰D. A. Fedosov, W. Pan, B. Caswell, G. Gompper, and G. E. Karniadakis, “Predicting human blood viscosity in silico,” *PNAS* **108**, 11772–11777 (2011).
- ²¹Z. Peng, X. Li, I. V. Pivkin, M. Dao, G. E. Karniadakis, and S. Suresh, “Lipid bilayer and cytoskeletal interactions in a red blood cell,” *PNAS* **110**, 13356–13361 (2013).
- ²²K. Kremer and G. S. Grest, “Dynamics of entangled linear polymer melts: A molecular-dynamics simulation,” *J. Chem. Phys.* **92**, 5057–5086 (1990).
- ²³J. Li, M. Dao, C. Lim, and S. Suresh, “Spectrin-level modeling of the cytoskeleton and optical tweezers stretching of the erythrocyte,” *Biophys. J.* **88**, 3707–3719 (2005).
- ²⁴M. Dao, J. Li, and S. Suresh, “Molecularly based analysis of deformation of spectrin network and human erythrocyte,” *Mater. Sci. Eng. C* **26**, 1232–1244 (2006), proceedings of the First TMS Symposium on Biological Materials Science.
- ²⁵G. Gompper and M. Schick, eds., “Soft matter, volume 4: Lipid bilayers and red blood cells,” (WILEY-VCH, 2008) Chap. Red Blood Cell Shapes and Transformations: Newtonian Mechanics of a Composite Membrane.
- ²⁶G. Gompper and D. M. Kroll, “Network models of fluid, hexatic and polymerized membranes,” *J. Phys. Condens. Matter* **9**, 8795 (1997).
- ²⁷N. Kaza, A. Ojaghi, and F. E. Robles, “Hemoglobin quantification in red blood cells via dry mass mapping based on UV absorption,” *J. Biomed. Opt.* **26**, 086501 (2021).

- ²⁸I. Moon, B. Javidi, F. Yi, D. Boss, and P. Marquet, “Automated statistical quantification of three-dimensional morphology and mean corpuscular hemoglobin of multiple red blood cells,” *Opt. Express* **20**, 10295–10309 (2012).
- ²⁹C. Humpert and M. Baumann, “Local membrane curvature affects spontaneous membrane fluctuation characteristics,” *Molecular Membrane Biology* **20**, 155–162 (2003).
- ³⁰Y.-Z. Yoon, H. Hong, A. Brown, D. C. Kim, D. J. Kang, V. L. Lew, and P. Cicuta, “Flickering analysis of erythrocyte mechanical properties: Dependence on oxygenation level, cell shape, and hydration level,” *Biophysical Journal* **97**, 1606–1615 (2009).
- ³¹H. Noguchi, “Swinging and synchronized rotations of red blood cells in simple shear flow,” *Phys. Rev. E* **80**, 021902 (2009).
- ³²J. L. McWhirter, H. Noguchi, and G. Gompper, “Flow-induced clustering and alignment of vesicles and red blood cells in microcapillaries,” *PNAS* **106**, 6039–6043 (2009).
- ³³N. S. Gov, “Active elastic network: Cytoskeleton of the red blood cell,” *Phys. Rev. E* **75**, 011921 (2007).
- ³⁴M. Takeuchi, H. Miyamoto, Y. Sako, H. Komizu, and A. Kusumi, “Structure of the erythrocyte membrane skeleton as observed by atomic force microscopy,” *Biophys. J.* **74**, 2171–2183 (1998).
- ³⁵A. H. Swihart, J. M. Mikrut, J. B. Ketterson, and R. C. Macdonald, “Atomic force microscopy of the erythrocyte membrane skeleton,” *J. Microsc.* **204**, 212–225 (2001).
- ³⁶D. A. Fedosov, *Multiscale modeling of blood flow and soft matter*, Ph.D. thesis, Brown University, Providence, RI (2010).